

The mass spectrum of the Schwinger model with Matrix Product States

M. C. Bañuls,^{1,*} K. Cichy,^{2,3} K. Jansen,^{2,4} and J. I. Cirac¹

¹*Max-Planck-Institut für Quantenoptik,*

Hans-Kopfermann-Str. 1, 85748 Garching, Germany

²*NIC, DESY Zeuthen, Platanenallee 6, 15738 Zeuthen, Germany*

³*Adam Mickiewicz University, Faculty of Physics,*

Umultowska 85, 61-614 Poznan, Poland

⁴*Department of Physics, University of Cyprus,*

P.O. Box 20537, 1678 Nicosia, Cyprus

(Dated: February 8, 2019)

Abstract

We show the feasibility of tensor network solutions for lattice gauge theories in Hamiltonian formulation by applying matrix product states algorithms to the Schwinger model with zero and non-vanishing fermion mass. We introduce new techniques to compute excitations in a system with open boundary conditions, and to identify the states corresponding to low momentum and different quantum numbers in the continuum. For the ground state and both the vector and scalar mass gaps in the massive case, the MPS technique attains precisions comparable to the best results available from other techniques.

*Electronic address: banulsm@mpq.mpg.de

I. INTRODUCTION

In the last years, methods based on tensor network states (TNS) have revealed themselves as very promising tools for the numerical study of strongly correlated quantum many-body systems. They are ansätze for the quantum state, characterized by their entanglement content and well suited for lattice systems. The paradigmatic family of TNS is that of matrix product states (MPS) [1–6], which underlies the well-known density matrix renormalization group algorithm (DMRG) [7, 8]. The enormous success of DMRG for the study of one dimensional condensed matter problems has been better understood within the framework of TNS (see e.g. [9]). This has also enabled different extensions of the original algorithm, such as time-dependence [10–12], so that MPS/DMRG methods constitute nowadays a quasi exact method for the study of ground states, low lying excitations and thermal equilibrium properties of quantum spin chains far beyond the reach of exact diagonalization. Being free from the sign problem which plagues quantum Monte Carlo (QMC) methods, higher dimensional TNS [13–15] are seen as powerful candidates for the numerical exploration of long standing strongly correlated electron problems.

This success has motivated the application of TNS techniques to further problems, and a relatively new field of application has been found in quantum field theories. Conformal Field Theory inspires a generalization of MPS [16] useful for critical models. Furthermore, specific generalizations of TNS exist [17–19] which are suitable for non-relativistic and relativistic QFT in the continuum. The discrete versions, on the other hand, are adequate for lattice field theories, and can in particular be applied to models relevant to high energy physics problems. This route was first explored using the original DMRG formulation [20, 21]. The deeper understanding of the technique achieved thanks to TNS has increased the power of these methods and new results are now available for critical QFT [22, 23].

A particularly interesting study case is that of the Schwinger model [24, 25], or QED in one spatial dimension, the simplest gauge theory, which nevertheless exhibits features in common with more complex models (QCD) such as confinement, a non-trivial vacuum and asymptotic freedom, and has been adopted as a benchmark model where to explore lattice gauge theory techniques (see e.g. [26–30] and references cited therein).

The application of MPS techniques to the Schwinger model was first explored by Byrnes et al. [20] using the original DMRG formulation. The study improved by several orders of

magnitude the precision attained by other Hamiltonian techniques for the ground state and the first (vector) mass gap, for vanishing and non-vanishing fermion masses, using periodic boundary conditions (PBC). However, DMRG estimations for higher excited states lose precision fast, in particular for PBC, and the scalar mass gap was not explored in [20].

In this paper we apply the more stable and numerically efficient MPS for open boundary conditions (OBC) to the same problem. We work in the subspace of physical states satisfying Gauss' law, in which the model can be written as a spin Hamiltonian with a long-range interaction [31, 32]. We improve the existing techniques to find higher excited states and devise a method to identify vector and scalar excitations in finite open chains, although the charge that distinguishes them is only a good quantum number in the continuum. We compute the ground state and the vector and scalar mass gaps for vanishing and non-vanishing fermion masses, with enough precision to conduct the extrapolation to the continuum limit. Our study shows the feasibility of TNS solutions for similar LGT, in the Hamiltonian formulation.

The rest of the paper is organized as follows. In section II we briefly introduce the Schwinger model, and review its formulation as a spin Hamiltonian. Section III presents the MPS formalism, with particular emphasis on the new techniques used to overcome the challenge posed by this particular kind of problems. In section IV we present our numerical results and conclude in section V with a discussion and outlook.

II. THE MODEL

The massive Schwinger model [24], or QED in two space-time dimensions, is a gauge theory, describing the interaction of a single fermionic species with the photon field, via the Lagrangian density,

$$\mathcal{L} = \bar{\Psi}(i\not{\partial} - g\not{A} - m)\Psi - \frac{1}{4}F_{\mu\nu}F^{\mu\nu}, \quad (1)$$

with $F_{\mu\nu} = \partial_\mu A_\nu - \partial_\nu A_\mu$, g is the coupling constant and m the fermion mass. The physics of the model is determined by the only dimensionless parameter m/g . The massless case, $m = 0$, can be solved analytically, via bosonization [24], and also the free case, $g = 0$, has exact solution, so that for very large or very small values of m/g a perturbative study is possible around one of the solvable limits, while in general a non-perturbative treatment may be needed. One of the features of the model is the existence of bound states, the two

lowest ones of which, the vector and the scalar, are stable for any value of m/g [25, 33].

The spectrum of the Schwinger model has been studied with many techniques. The most accurate numerical estimations have been performed on the lattice. For the vector mass the best results were obtained with DMRG [20], while strong coupling expansion (SCE) got the most accurate prediction for the scalar mass [34, 35] and the most precise values in the massless case [36].

In the temporal gauge, $A_0 = 0$, the Hamiltonian density reads

$$\mathcal{H} = -i\bar{\Psi}\gamma^1(\partial_1 - igA_1)\Psi + m\bar{\Psi}\Psi + \frac{1}{2}E^2. \quad (2)$$

The electric field, $E = -\dot{A}^1$, is fixed by the additional constraint of Gauss' law, $\partial_1 E = g\bar{\Psi}\gamma^0\Psi$, up to a constant of integration, which can be interpreted as a background field [25].

The model can be formulated on a lattice. Here we focus on the Kogut-Susskind staggered formulation [37],

$$H = -\frac{i}{2a} \sum_n (\phi_n^\dagger e^{i\theta_n} \phi_{n+1} - \text{h.c.}) + m \sum_n (-1)^n \phi_n^\dagger \phi_n + \frac{ag^2}{2} \sum_n L_n^2, \quad (3)$$

where a is the lattice spacing. We consider a lattice with open boundaries, with sites $n = 0, \dots, N - 1$. On each site there is a single-component fermion field ϕ_n , while θ_n are the gauge variables sitting on the links between n and $n + 1$, and connected to the vector potential via $\theta_n = -aqA_n^1$. L_n is the corresponding conjugate variable, $[\theta_n, L_m] = i\delta_{nm}$, connected to the electric field as $gL_n = E_n$. We work in a compact formulation, where θ_n becomes an angular variable, and L_n can adopt integer eigenvalues. Gauss' law appears as the additional constraint

$$L_n - L_{n-1} = \phi_n^\dagger \phi_n - \frac{1}{2} [1 - (-1)^n]. \quad (4)$$

Instead of the Hamiltonian (3), it is usual to work with the dimensionless operator $W = \frac{2}{ag^2}H$, and to define parameters $x = \frac{1}{g^2a^2}$ and $\mu = \frac{2m}{g^2a}$. In this picture, fermions on even and odd sites respectively correspond to the upper and lower components of the spinor representing the fermionic field in the continuum. Gauss' law (4) determines the electric field up to a constant α which can be added to L_n and represents the background electric field.

Using a Jordan-Wigner transformation, $\phi_n = \prod_{k<n} (i\sigma_k^z)\sigma_n^-$, where $\sigma^\pm = \sigma^x \pm i\sigma^y$, model (3) can be mapped to a spin Hamiltonian [31],

$$H = x \sum_{n=0}^{N-2} [\sigma_n^+ \sigma_{n+1}^- + \sigma_n^- \sigma_{n+1}^+] + \frac{\mu}{2} \sum_{n=1}^N [1 + (-1)^n \sigma_n^z] + \sum_{n=0}^{N-2} (L_n + \alpha)^2. \quad (5)$$

Gauss' law reads then $L_n - L_{n-1} = \frac{1}{2} [\sigma_n^z + (-1)^n]$, and can be used to eliminate the gauge degrees of freedom, leaving the Hamiltonian [38]

$$H = x \sum_{n=0}^{N-2} [\sigma_n^+ \sigma_{n+1}^- + \sigma_n^- \sigma_{n+1}^+] + \frac{\mu}{2} \sum_{n=1}^N [1 + (-1)^n \sigma_n^z] + \sum_{n=0}^{N-2} \left[\ell + \frac{1}{2} \sum_{k=0}^n ((-1)^k + \sigma_k^z) \right]^2, \quad (6)$$

where ℓ is the boundary electric field, on the link to the left of site 0, which can describe the background field.

A useful basis for this problem is then

$$|\ell\rangle \otimes |i_0 i_1 \dots i_{N-2} i_{N-1}\rangle, \quad (7)$$

with $i_m = \{0, 1\}$ labeling the ± 1 eigenstates of σ_m^z (on site m). An even site in spin state $|1\rangle$ corresponds to the presence of a fermion, while an odd site in state $|0\rangle$ is an antifermion at the corresponding position. The integer valued $\ell = \dots, -1, 0, 1, \dots$ is the only gauge degree of freedom left, but with OBC it is non-dynamical, as the Hamiltonian cannot connect states with different values of ℓ . Here we choose $\ell = 0$ and omit it in the following, as we will be concerned with the case of zero background field. Moreover, we are interested in states with zero total charge ($\sum_n \sigma_n^z = 0$ in the spin language), so we consider chains with even N .

III. METHOD

In this work we use the MPS ansatz to approximate the ground and lowest excited states of the Hamiltonian (6). A MPS for a system of N d -dimensional sites has the form $|\Psi\rangle = \sum_{i_1, \dots, i_N=1}^d \text{tr}(A_1^{i_1} \dots A_N^{i_N}) |i_1, \dots, i_N\rangle$, where $\{|i\rangle\}_{i=0}^{d-1}$ are individual basis states for each site. Each A_k^i is a D -dimensional matrix and the bond dimension, D , determines the number

of parameters in the ansatz. MPS are known to provide good approximations to ground states of local Hamiltonians in the gapped phase, but have also been successfully used for more general models.

The MPS approximation to the ground state can be found variationally by successively minimizing the energy, $\frac{\langle \Psi | H | \Psi \rangle}{\langle \Psi | \Psi \rangle}$, with respect to each tensor A_k until convergence. Each such optimization reduces to the eigenvalue problem of an effective Hamiltonian that acts on site k and its adjacent virtual bonds. The basic algorithm, closely related to the original DMRG formulation [7, 8], was introduced in [5], and is nowadays widely used.

In DMRG it is possible to target several of the lowest eigenstates [40], or, in the case of a first excited state with a distinct quantum number, to run the ground state search in different sectors. In the MPS formalism, it is natural to extend the variational method to determine excited states by performing a constrained minimization which imposes orthogonality with respect to the already computed states (ground and lower excited states), as proposed in [41] and recently extended in [42]. Here we introduce a simpler variation of the ground state algorithm, which allows us to compute MPS approximations to the lowest energy eigenstates at lower cost, without using any explicit symmetry. This is especially interesting for a finite system with open boundary conditions, where momentum is not a good quantum number. It is worth noticing that in the case of translationally invariant (TI) systems, either finite and periodic or infinite, a very successful approach exists based on the construction of well-defined momentum MPS [43].

For finite systems, the MPS algorithms for open boundary conditions are numerically more stable and in general more efficient, although improved methods have been recently proposed for periodic systems [44, 45]. However, finite-size effects are much larger for OBC and therefore simulation of larger chains may be needed to reach the thermodynamic limit reliably.

To determine the first excited state, after having found the ground state of the system, $|\Psi_0\rangle$, we can construct the projector onto the orthogonal subspace, $\Pi_0 = 1 - |\Psi_0\rangle\langle\Psi_0|$. The first excitation corresponds then to the state that minimizes the energy of the projected Hamiltonian,

$$E_1 = \min_{|\Psi\rangle} \frac{\langle \Psi | \Pi_0 H \Pi_0 | \Psi \rangle}{\langle \Psi | \Psi \rangle} = \frac{\langle \Psi | (H - E_0 |\Psi_0\rangle\langle\Psi_0|) | \Psi \rangle}{\langle \Psi | \Psi \rangle}, \quad (8)$$

given that $E_1 < 0$, what we can always ensure by adding an appropriate constant to H . This minimization corresponds to finding the ground state of the effective Hamiltonian

$H_{\text{eff}}[1] = \Pi_0 H \Pi_0$. The procedure can be concatenated to find subsequent energy levels, so that, to find the M -th excited state, we will search for the ground state of the Hamiltonian

$$\begin{aligned} H_{\text{eff}}[M] &= \Pi_{M-1} \dots \Pi_0 H \Pi_0 \dots \Pi_{M-1} \\ &= H - \sum_{k=0}^{M-1} E_k |\Psi_k\rangle \langle \Psi_k|. \end{aligned} \quad (9)$$

Each of these ground state searches can be solved by applying the standard variational MPS algorithm to the corresponding effective Hamiltonian (9), which can be constructed from the set of all previously computed MPS levels $\{|\Psi_k\rangle\}$. The expression to be minimized at each step of the MPS iteration is then $\min_{A_k} \frac{A_k^* \mathcal{H}_k A_k}{A_k^* \mathcal{N}_k A_k}$, where \mathcal{H}_k and \mathcal{N}_k are the effective Hamiltonian and norm matrix acting on site k and its two adjacent virtual bonds, so that each tensor can be found by solving a generalized eigenvalue problem $\mathcal{H}_k A_k = \lambda \mathcal{N}_k A_k$. As illustrated in figure 1, \mathcal{H}_k and \mathcal{N}_k are computed by contracting all tensors but A_k , and the computational cost can be optimized, as in the original algorithm, by storing and reusing the partial contractions that compose these effective matrices. In general this is most easily done when all the terms in the problem Hamiltonian are expressed as a matrix product operator (MPO) [46]. In this particular case it is more convenient to keep separate temporary terms for each of the contractions $\langle \Psi_k | \Psi \rangle$, and to reconstruct from them the effective projectors on every site, before constructing the effective Hamiltonian. In this way, the computational cost for each such term scales as dD^3 , without increasing the leading cost of the algorithm. Due to the larger number of terms that need to be kept, however, the cost of finding the M -th level once all the lower ones are known will be about M times higher than that of the original ground state search [50], and thus the total cost for computing up to the M -th level will scale as $M^2 D^3$.

The masses of the particles in the theory are given by the energies of the zero momentum excitations. In finite systems with OBC momentum is difficult to identify and we need to find the excitations that will correspond to the lowest momentum in the continuum limit. In dynamical DMRG [47] momentum dependent quantities were extracted from finite DMRG calculations with open boundaries using quasimomentum states defined from the eigenstates of a free particle in a box. Here we use a different approach, based on the continuum momentum operator for the fermion field, $\hat{P} = \int dx \Psi^\dagger(x) i \partial_x \Psi(x)$. Its discretization yields,

in the spin representation, and after rescaling by a factor $\frac{2}{ag^2}$, the operator

$$\hat{O}_P = -ix \sum_n [\sigma_n^- \sigma_{n+1}^z \sigma_{n+2}^+ - h.c.]. \quad (10)$$

The expectation values of \hat{O}_P^2 can be used to assign a pseudo-momentum to the spectral levels, in order to reconstruct the dispersion relation (Fig. 2).

The model gives rise to stable particles, the lowest ones being, in the case of no background field, the *vector* and *scalar* states. In the continuum model, these particles are distinguished by well-defined parity and charge conjugation quantum numbers [25], with the scalar living in the same sector as the ground state. On a staggered lattice with PBC it is possible to exploit the corresponding lattice symmetries to construct two orthogonal subspaces respectively containing the vector, and the ground state with the scalar [48]. For a chain with OBC the number of surviving symmetries is even lower, with translational invariance lost. In practice this means that to calculate the scalar mass, we need to identify first the momentum excitations of the vector, which appear at lower energy than the scalar. In [38] this was done by starting from the strong coupling limit ($x \rightarrow 0$), where vector and scalar states are known exactly, and smoothly changing the x parameter while keeping a label on the scalar state. Instead, we use the expectation value of the spin transformation, $S_R = \otimes_{k=0}^{N-1} \sigma_{2k-1}^x T^{(1)}$, where $T^{(1)}$ is the (cyclic) translation by one spin site [51]. In a system with PBC this operator basically describes the action of charge conjugation on the spins, with the translation exchanging the fermionic and antifermionic character of sites, and the σ_x rotation accounting for the different meaning of a spin *up* on an even (fermion) site (empty) and on an odd one (occupied). Charge conjugation is a good quantum number and distinguishes the vector state ($C = -1$) from the sector containing the scalar and the ground state ($C = +1$), even for finite systems. On the staggered lattice with OBC this is no longer true, and S_R does not commute with the Hamiltonian. However the phase of S_R keeps memory of this distinction, and allows us to tag the levels accordingly, with the ground state and the scalar branch of the dispersion relation having phase $\varphi(\langle S_R \rangle) \approx 0$ and the vector branch $\varphi(\langle S_R \rangle) \approx \pi$, as illustrated in figure 2.

IV. RESULTS

We have applied the methods described in section III to the Hamiltonian (6) to determine the ground state, and the vector and scalar mass gaps for different values of the fermion mass. In order to benchmark our results with existing data, we have studied different masses $m/g = 0, 0.125, 0.25$ and 0.5 , for which reference values can be found in the literature.

The continuum limit corresponds to the lattice spacing $a \rightarrow 0$, or $x \rightarrow \infty$. The goal is then to compute the ground state energy density, and the vector and scalar mass gaps in the thermodynamic limit ($N \rightarrow \infty$) for different finite values of x , and to extrapolate them to the continuum limit. We have used values of $x \in [5, 600]$. In order to extract the thermodynamic limit for each case, we need to simulate different system sizes, N , and apply some finite-size scaling. The system sizes, N , cannot be chosen independently of the value of x , as the same number of sites N corresponds to different physical volumes $L_{\text{phys}} = Na$ for different values of $x \propto 1/a^2$. From numerical simulations, we estimated that choosing $N \geq 20\sqrt{x}$ ensures small enough finite volume effects. We thus study for each value of x 3-4 different system sizes, large enough for the condition above to be satisfied (for instance, for $x = 5$ we take $N \in [68, 82]$ while for $x = 600$, $N \in [736, 834]$). For each of them, we have run the MPS algorithms for the ground state and excited states, described in the previous section, with bond dimensions $D \in [20, 140]$, at least until a candidate scalar state is found. We are interested in the subspace of null total charge, which corresponds to $\sum S_z = 0$. This can easily be imposed by adding a penalty term to the Hamiltonian. Since the computation time increases with N and D , for some of the larger chains not all the bond dimensions are calculated. For every level, the MPS iteration stops when the relative change in the energy after one full sweep over the chain is below a certain tolerance, ϵ . The value of ϵ has to be small to ensure a good precision after the extrapolations, but a smaller tolerance translates in more difficult convergence. Therefore we fixed $\epsilon = 10^{-12}$ for the ground state and the vector calculations, and $\epsilon = 10^{-7}$ for the longer computations needed for the scalar states.

For each set of parameters $(m/g, x, L)$ and for each of the levels we are interested in, we extrapolate our results to $1/D \rightarrow 0$. For the ground state and the vector state, almost all the bond dimensions are converged, while for the scalar mass gap, depending on a larger number of intermediate excited states, some of the larger systems are only computed with smaller bond dimension. In each case, we extrapolate linearly in $1/D$ from the largest bond

dimensions available in the data (in the cases when the scalar is only available for a small $D \leq 80$, we take the value corresponding to the largest D as our estimation for the energy, and estimate the error as the difference between this value and the one for the immediately smaller D). In figure 3 we show the results of this step for one particular case.

The results of the extrapolation described above provide accurate estimators for the energy levels for various finite chains. We then proceed to scale these results with finite-size to extract the ground state energy density, $E_0/(2xN)$, and the mass gaps, $(E_{1(2)} - E_0)/(2\sqrt{x})$ in the thermodynamic limit for each pair of parameters $(m/g, x)$. Finite-size corrections to the ground state energy density are linear in $1/N$, while for the energy gaps, the leading corrections arise from a kinetic energy term $O(\pi/N^2)$ [38]. Hence the bulk limit is extracted by fitting the ground state energy density as

$$\frac{E_0}{2xN} \approx \omega_0 + \frac{\alpha}{N} + \frac{\beta}{N^2}, \quad (11)$$

and the energy gaps as

$$\frac{E_{1(2)} - E_0}{2\sqrt{x}} \approx \omega_{1(2)} + \frac{\alpha_{1(2)}}{N^2} + O\left(\frac{1}{N^3}\right). \quad (12)$$

We have run these fits for each pair of values $(m/g, x)$, as illustrated in figure 4 for a particular case.

Finally, the values in the continuum limit can be extracted from the ones in the thermodynamic limit by fitting them, for each value of the mass, to a polynomial in $\frac{1}{\sqrt{x}}$. For these fits, we include only those values of x for which the thermodynamic limit can be extracted accurately (i.e. the corresponding level for the various system sizes is converged to a large enough D). The continuum limit extrapolations are shown in figures 5 (ground state), 6 (vector) and 7 (scalar). The interval $[x_{\min}, x_{\max}]$ and the function used for the fit affect the final result. We have thus used a quadratic function in $\frac{1}{\sqrt{x}}$, $A + \frac{B}{\sqrt{x}} + \frac{C}{x}$ and performed the fit over various intervals. We choose as our final estimation the value obtained from the best fit, and estimate the error from the difference with respect to another interval (see figure captions).

Finally, we obtain for the ground state energy density in the massless case the value $\omega_0 = -0.31837(7)$, to be compared to the exact value, $-1/\pi \approx -0.3183099$. Our result for the ground state energy in the massive cases is independent of m/g , as expected [34]. The results for the vector binding energies, $\frac{M_V}{g} := \omega_1 - 2m/g$, are shown in the following table

for each value of m/g studied, with the DMRG estimates [20] shown for comparison. In the massless case, the exact value is also displayed.

	Vector binding energy		
m/g	MPS with OBC	DMRG result [20]	exact
0	0.5642(2)	0.5642(2)	0.5641895
0.125	0.53951(16)	0.53950(7)	-
0.25	0.5192(5)	0.51918(5)	-
0.5	0.48742(13)	0.48747(2)	-

For the scalar binding energy, $\frac{M_S}{g} := \omega_2 - 2m/g$, the most precise results found in the literature, for the massive case, correspond to the strong coupling expansion [35]. Again, we show them together with our best fit and the exact value for the massless case in the following table.

	Scalar binding energy		
m/g	MPS with OBC	SCE result [35]	exact
0	1.1283(10)	1.11(3)	1.12838
0.125	1.221(2)	1.22(2)	-
0.25	1.239(6)	1.24(3)	-
0.5	1.213(5)	1.20(3)	-

One of the factors explaining the lower precision attained in the scalar calculation as compared to the vector results, is the longer time required to reach the scalar state with the MPS algorithm for excited states. As discussed in section III the computational cost scales like the square of the required number of levels. Since in many instances the first scalar candidate appears at level 10 or above, this represents a cost about 100 times larger than in the case of the ground state. We have thus opted for a trade-off between precision and efficiency, and have applied in this case a less demanding convergence criterion than in the case of the vector or the ground state, what also translates in less precision in the final results. The less precise finite-size scalings also correspond to the same reason, as the largest bond dimensions are in some cases not available.

V. DISCUSSION

We have successfully employed open boundary MPS to compute the ground state and several excited levels of the lattice Schwinger model, using a staggered formulation, and for various values of the fermion mass. Although in the physical subspace in which we work the model contains long range interactions which do not decay with the distance, we have found that MPS produce a very good approximation not only to the ground state, but also to higher excited levels and we are able to reach precisions comparable (or for the case of the scalar even slightly better) to those available from other techniques. Additionally, the precision we reach is not extremely sensitive to the value of the mass, what further points to the usefulness of TN techniques for the non-perturbative parts of the parameter space.

Our results validate the usefulness of tensor network techniques, in particular MPS, for lattice gauge theory problems. We have obtained very precise results, even though the open boundary MPS cannot represent states with well-defined momentum, a problem that a TI ansatz might likely overcome. MPS, and in more generality TNS, seem thus to be a promising tool to deal also with models that have open boundary conditions, as is now advocated for QCD [49].

In order to determine the mass gaps, we have also extended the MPS tools to approximate excited states, and we have proposed a modified algorithm that is efficient and allows us to approximate more than ten excited states in chains of hundreds of sites.

One of the main advantages of the MPS methods used in this work is that they easily allow us to attack other problems which are more complicated for standard lattice techniques. In particular, we can trivially include a chemical potential term in the Hamiltonian, and we can easily study thermal equilibrium properties. It is also possible to simulate real time evolution, which opens the door to out-of-equilibrium questions. Additionally, we could perform a similar study in a more complicated lattice theory, in particular with a non-Abelian symmetry, getting in this way closer to the target of lattice QCD studies. Thus, although tensor networks are presently not competitive with standard Monte Carlo techniques for 4D quantum field theories, they might allow us to address problems that are not amenable for customary lattice field theory techniques.

Acknowledgments

This work was partially funded by the EU through SIQS grant (FP7 600645). K.C. was supported by Foundation for Polish Science fellowship “Kolumb”. This work was supported in part by the DFG Sonderforschungsbereich/Transregio SFB/TR9. K.J. was supported in part by the Cyprus Research Promotion Foundation under contract ΠΡΟΣΕΛΚΥΣΗ/ΕΜΠΕΙΡΟΣ/0311/16.

- [1] I. Affleck, T. Kennedy, E. H. Lieb, and H. Tasaki, *Commun. Math. Phys.*, **115**, 477 (1988).
- [2] A. Klumper, A. Schadschneider, and J. Zittartz, *J. Phys. A*, **24**, L955 (1991).
- [3] A. Klumper, A. Schadschneider, and J. Zittartz, *Z. Phys. B*, **87**, 281 (1992).
- [4] M. Fannes, B. Nachtergaele, and R. F. Werner, *Commun. Math. Phys.*, **144**, 443 (1992).
- [5] F. Verstraete, D. Porras, and J. I. Cirac, *Phys. Rev. Lett.*, **93**, 227205 (2004).
- [6] D. Perez-García, F. Verstraete, M. M. Wolf, and J. I. Cirac, *Quantum Inf. Comput.*, **7**, 401 (2007).
- [7] S. R. White, *Physical Review Letters*, **69**, 2863 (1992).
- [8] U. Schollwöck, *Rev. Mod. Phys.*, **77**, 259 (2005).
- [9] U. Schollwöck, *Annals of Physics*, **326**, 96 (2011).
- [10] G. Vidal, *Phys. Rev. Lett.*, **91**, 147902 (2003).
- [11] A. J. Daley, C. Kollath, U. Schollwöck, and G. Vidal, *J. Stat. Mech.*, **2004**, P04005 (2004).
- [12] G. Vidal, *Phys. Rev. Lett.*, **98**, 070201 (2007).
- [13] F. Verstraete and J. I. Cirac, (2004), cond-mat/0407066 .
- [14] G. Vidal, *Phys. Rev. Lett.*, **99**, 220405 (2007).
- [15] J. I. Cirac and F. Verstraete, *Journal of Physics A: Mathematical and Theoretical*, **42**, 504004 (2009).
- [16] J. I. Cirac and G. Sierra, *Phys. Rev. B*, **81**, 104431 (2010).
- [17] F. Verstraete and J. I. Cirac, *Phys. Rev. Lett.*, **104**, 190405 (2010).
- [18] T. J. Osborne, J. Eisert, and F. Verstraete, *Phys. Rev. Lett.*, **105**, 260401 (2010).
- [19] J. Haegeman, T. J. Osborne, H. Verschelde, and F. Verstraete, *Phys. Rev. Lett.*, **110**, 100402 (2013).

- [20] T. M. R. Byrnes, P. Sriganesh, R. J. Bursill, and C. J. Hamer, Phys. Rev. D, **66**, 013002 (2002).
- [21] T. Sugihara, Journal of High Energy Physics, **2005**, 022 (2005).
- [22] D. J. Weir, Phys. Rev. D, **82**, 025003 (2010).
- [23] A. Milsted, J. Haegeman, and T. J. Osborne, “Matrix product states and variational methods applied to critical quantum field theory,” (2013), arXiv:1302.5582 [hep-lat] .
- [24] J. Schwinger, Phys. Rev., **128**, 2425 (1962).
- [25] S. Coleman, Annals of Physics, **101**, 239 (1976), ISSN 0003-4916.
- [26] C. Gutfeld, H. Kastrup, and K. Stergios, Nucl.Phys., **B560**, 431 (1999), arXiv:hep-lat/9904015 [hep-lat] .
- [27] C. Gattringer, I. Hip, and C. Lang, Phys.Lett., **B466**, 287 (1999), arXiv:hep-lat/9909025 [hep-lat] .
- [28] L. Giusti, C. Hoelbling, and C. Rebbi, Phys.Rev., **D64**, 054501 (2001), arXiv:hep-lat/0101015 [hep-lat] .
- [29] N. Christian, K. Jansen, K. Nagai, and B. Pollakowski, Nucl.Phys., **B739**, 60 (2006), arXiv:hep-lat/0510047 [hep-lat] .
- [30] W. Bietenholz, I. Hip, S. Shcheredin, and J. Volkholz, Eur.Phys.J., **C72**, 1938 (2012), arXiv:1109.2649 [hep-lat] .
- [31] T. Banks, L. Susskind, and J. B. Kogut, Phys.Rev., **D13**, 1043 (1976).
- [32] D. Crewther and C. Hamer, Nuclear Physics B, **170**, 353 (1980), ISSN 0550-3213.
- [33] C. Adam, Annals of Physics, **259**, 1 (1997), ISSN 0003-4916.
- [34] C. Hamer, J. Kogut, D. Crewther, and M. Mazzolini, Nuclear Physics B, **208**, 413 (1982), ISSN 0550-3213.
- [35] P. Sriganesh, C. J. Hamer, and R. J. Bursill, Phys. Rev. D, **62**, 034508 (2000).
- [36] K. Cichy, A. Kujawa-Cichy, and M. Szyniszewski, Computer Physics Communications, **184**, 1666 (2013), ISSN 0010-4655.
- [37] J. Kogut and L. Susskind, Phys. Rev. D, **11**, 395 (1975).
- [38] C. J. Hamer, Z. Weihong, and J. Oitmaa, Physical Review D, **56**, 55 (1997).
- [39] F. Verstraete, V. Murg, and J. Cirac, Advances in Physics, **57**, 143 (2008).
- [40] K. A. Hallberg, Advances in Physics, **55**, 477 (2006).
- [41] D. Porras, F. Verstraete, and J. I. Cirac, Phys. Rev. B, **73**, 014410 (2006).

- [42] M. L. Wall and L. D. Carr, *New Journal of Physics*, **14**, 125015 (2012).
- [43] J. Haegeman, B. Pirvu, D. J. Weir, J. I. Cirac, T. J. Osborne, H. Verschelde, and F. Verstraete, *Physical Review B*, **85**, 100408 (2012).
- [44] P. Pippin, S. R. White, and H. G. Evertz, *Phys. Rev. B*, **81**, 081103 (2010).
- [45] B. Pirvu, F. Verstraete, and G. Vidal, *Phys. Rev. B*, **83**, 125104 (2011).
- [46] B. Pirvu, V. Murg, J. I. Cirac, and F. Verstraete, *New Journal of Physics*, **12**, 025012 (2010).
- [47] E. Jeckelmann, *Physical Review B*, **66**, 045114 (2002).
- [48] T. Banks, L. Susskind, and J. Kogut, *Phys. Rev. D*, **13**, 1043 (1976).
- [49] M. Luscher and S. Schaefer, *JHEP*, **1107**, 036 (2011), arXiv:1105.4749 [hep-lat] .
- [50] This refers only to the leading computational cost, as in some cases convergence of a particular excited states may result slower due to small gaps.
- [51] The choice of a cyclic translation ensures unitarity of the operator, and is irrelevant in the thermodynamic limit.

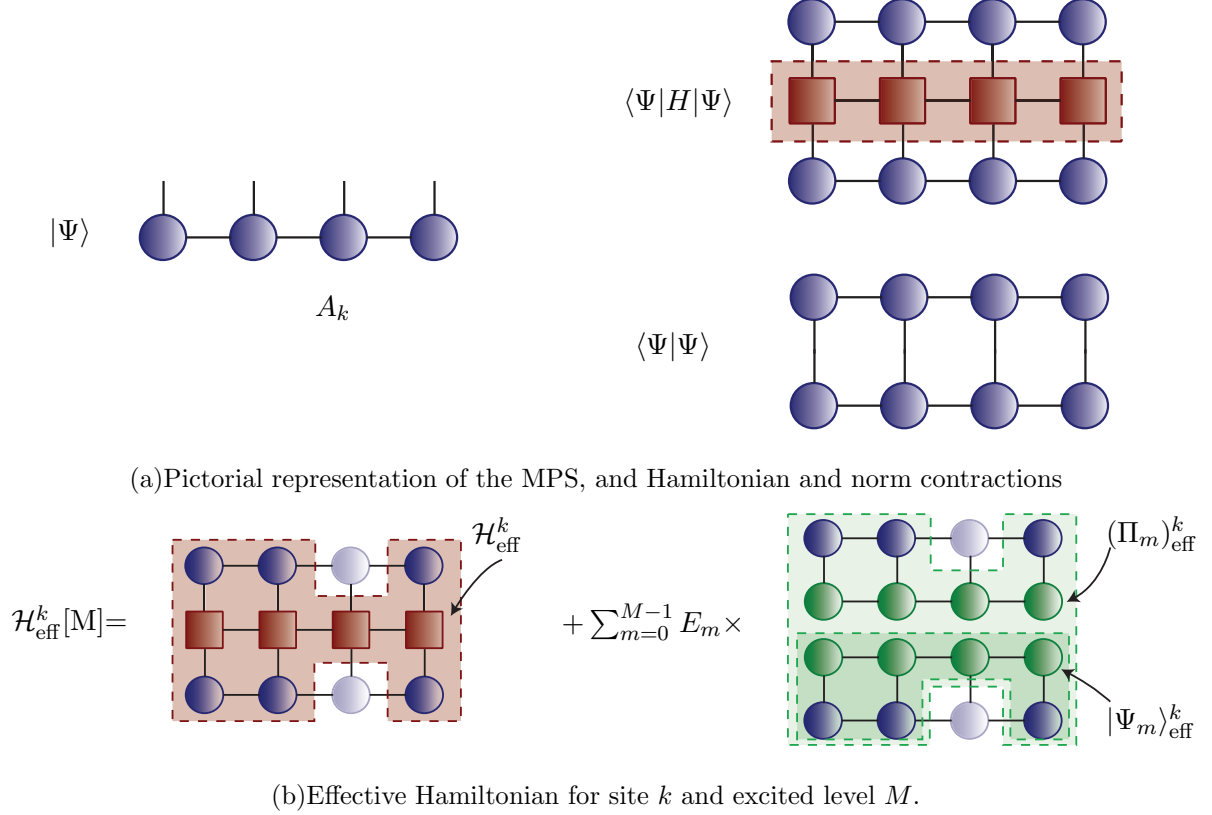


FIG. 1: Scheme of the algorithm for excited states. In 1(a) (left) we show the commonly used graphical representation of a MPS (see e.g. [39]). Each circle corresponds to one tensor (A_k) and each of its legs represents one index, with lines that join two tensors representing a contracted index (as in a matrix multiplication). The open legs correspond to the physical indices on each site. A particular coefficient in the product basis corresponds to fixing each of the open indices to a value $(0, \dots, d-1)$. On the right, we show the representation of some usual contractions. We can contract two MPS by joining their open (physical) indices to compute the norm (lower scheme) or insert an operator with a matrix product structure, as the Hamiltonian, to obtain the expectation value of the energy (above). In 1(b) we show the tensor network representation of \mathcal{H}_k in the step of the optimization where site k is computed. The term on the left is simply the contraction of the TN for $\langle H \rangle$ except for tensor A_k . Each term in the sum on the right is the TN for the expectation value of one projector ($\langle \Psi | \Psi_m \rangle \langle \Psi_m | \Psi \rangle$) leaving out the tensor at site k . The sum of all these terms produces the effective Hamiltonian at site k .

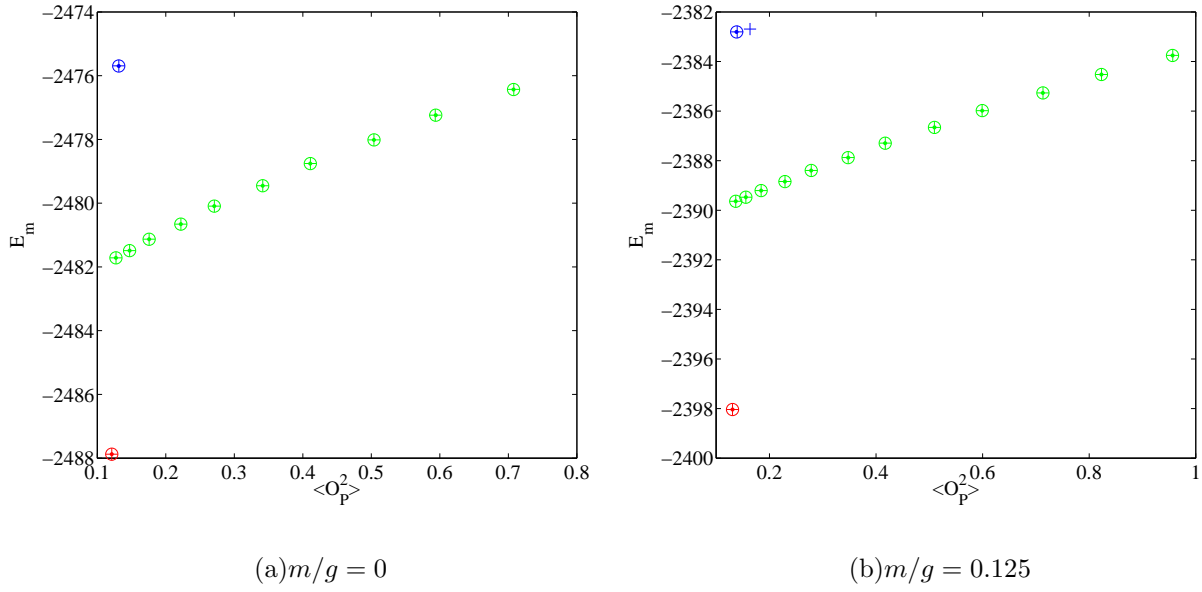


FIG. 2: Dispersion relation (energy vs. $\langle O_P^2 \rangle$) obtained with MPS for $x = 25$, $N = 160$ and $m/g = 0$ (left) and $m/g = 0.125$ (right). Shown are the states reconstructed with bond dimensions $D = 40$ (crosses), 80 (circles) and 100 (dots) (being on top of each other in the graph) until we have reached a scalar candidate. The appearance of the scalar is detected by the phase of the expectation value $\langle S_R \rangle$, with the scalar (indicated in blue in the plots) being the first state with $\varphi \approx 0$ above the ground state (red) while states with $|\varphi| \approx \pi$ belong to the vector branch (green).

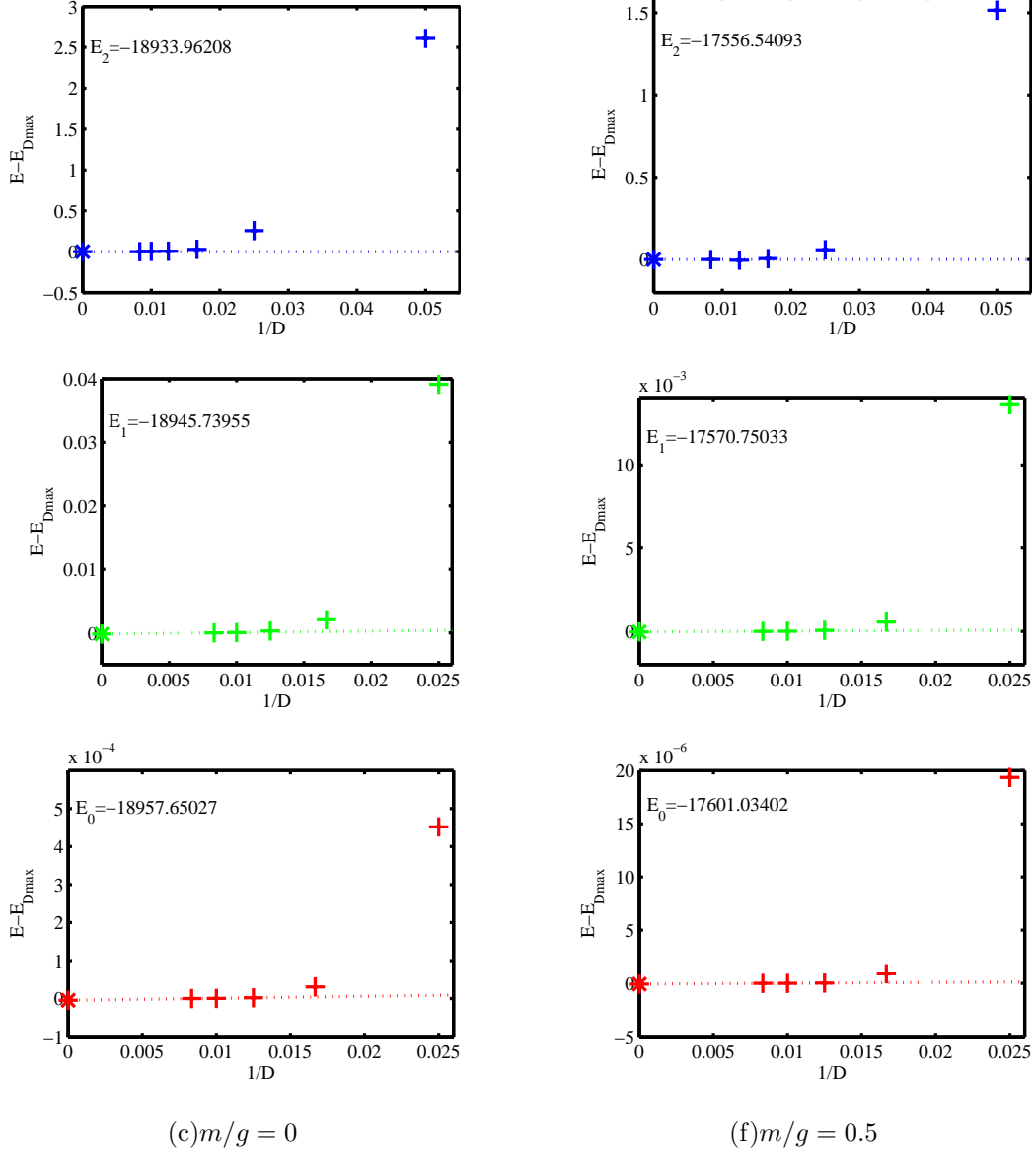


FIG. 3: Convergence of the energy levels with the bond dimension, D , for $x = 100$ and $N = 300$. In the left column, we show the results of the scalar (uppermost plot, blue), vector (middle plot, green) and ground state (lowest plot, red) for the massless case, $m/g = 0$, while the right column contains the corresponding results for the case $m/g = 0.5$. Plotted is the difference between the computed energy at a certain bond dimension and the one for the maximum D_{\max} . The error bars (smaller than the marker size) indicate the convergence criterion of the MPS algorithm, ($\epsilon = 10^{-7}$ for the scalar and 10^{-12} for the rest). Dashed lines show the extrapolation in $1/D$, with the final value displayed as a star (numerical value inside each panel). In the case of the ground state, we extrapolate linearly from the three largest values of D . For the vector, converging slower, we use the last two values, and for the scalar we take as our estimate the value given by the largest D .

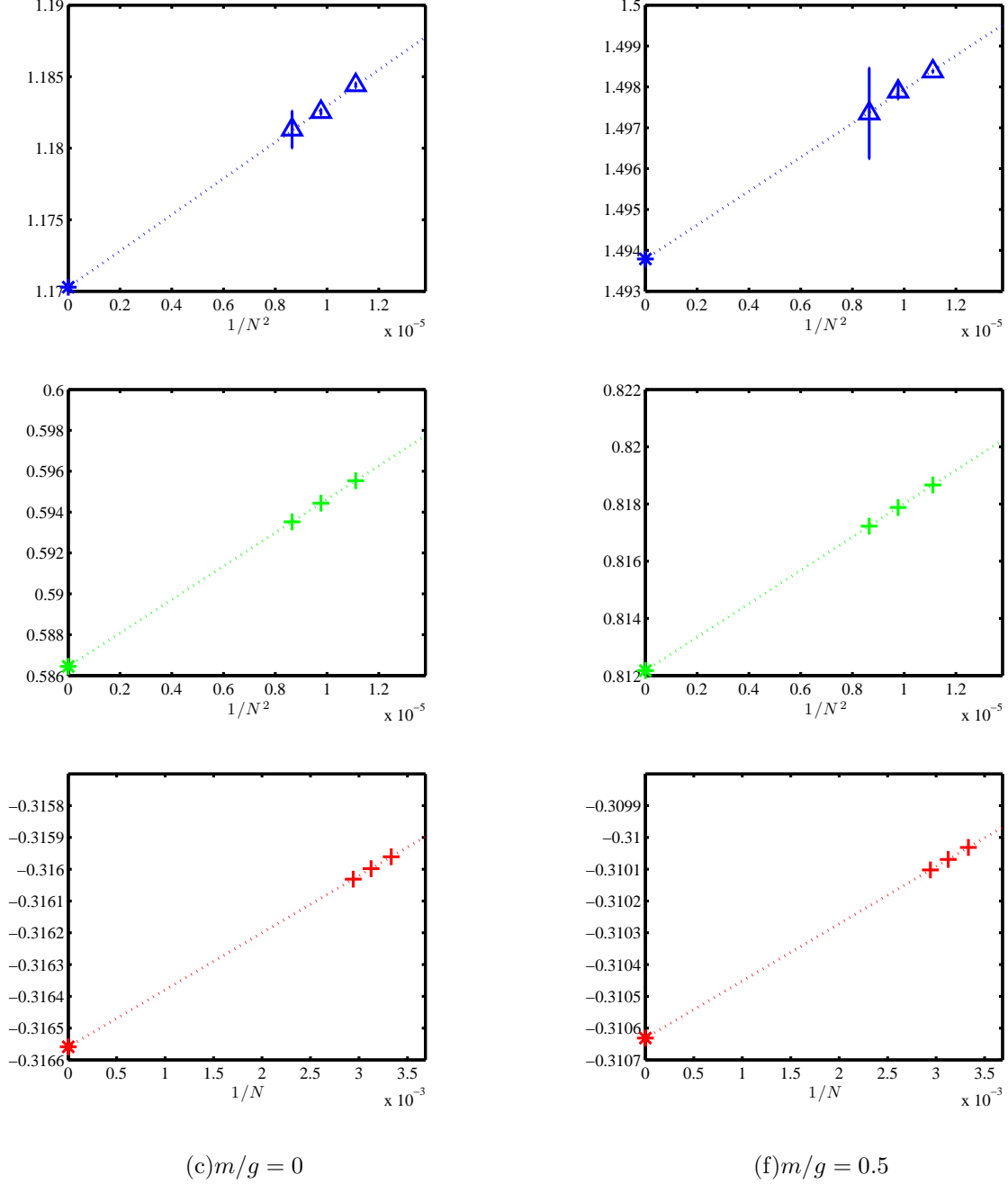
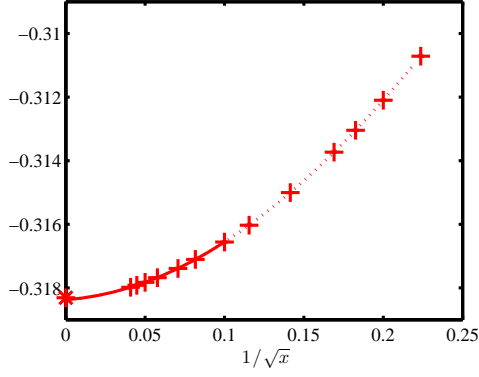
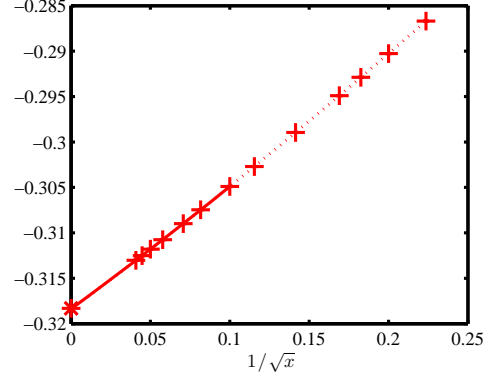


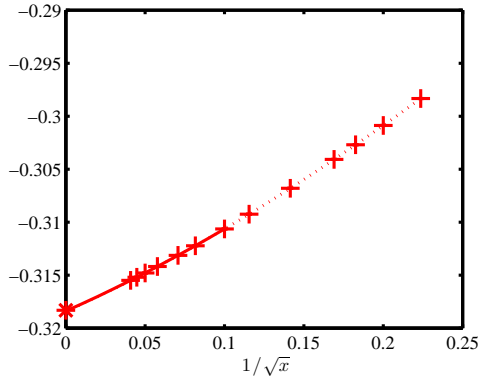
FIG. 4: Finite size scaling for $x = 100$ and mass $m/g = 0$ (left column) and $m/g = 0.125$ (right column). The two uppermost rows show as a function of $1/N^2$ the values obtained for finite systems for the scalar (blue) and vector (green) mass gaps, $\frac{E_{2(1)} - E_0}{2\sqrt{x}}$. The dashed line corresponds to the fit (12), with the resulting value indicated on the axis. The lowest row corresponds to the ground state energy density, $\frac{E_0}{2xN}$, as a function of $1/N$, and is fitted according to (11). Notice that the lattice sizes are already close to the thermodynamic limit. The error bars are extracted from the extrapolation in D , shown in figure 3.



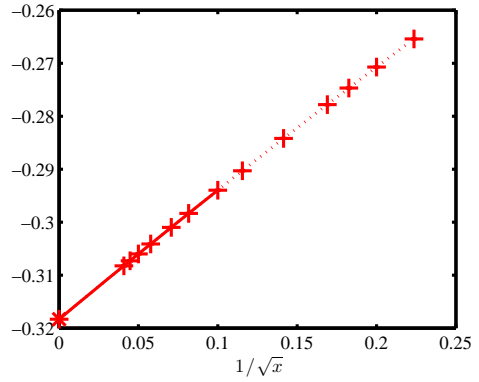
(a) $m/g = 0$, $\omega_0 = -0.31837(7)$



(c) $m/g = 0.25$, $\omega_0 = -0.31837(9)$

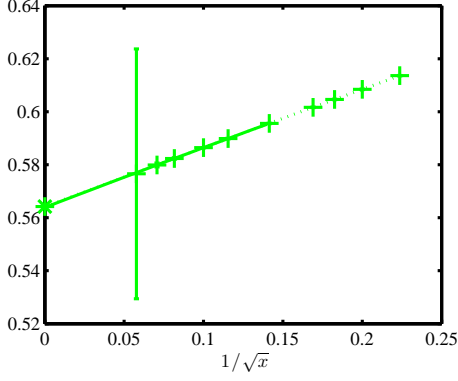


(b) $m/g = 0.125$, $\omega_0 = -0.31838(8)$

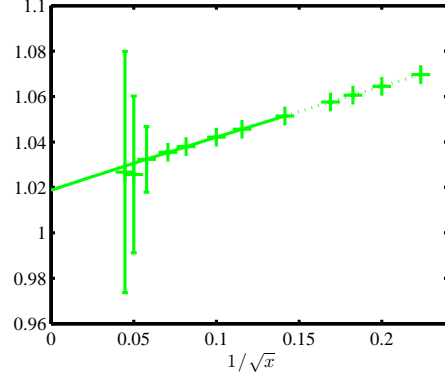


(d) $m/g = 0.5$, $\omega_0 = -0.31830(1)$

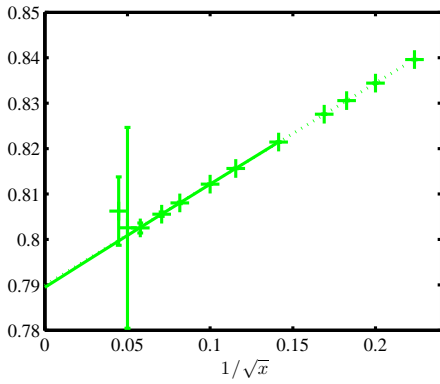
FIG. 5: Ground state energy density as a function of $1/\sqrt{x}$. The error bars show the uncertainties of the linear fits (11), and the star on the vertical axes indicates the (exact) solution for the massless theory, $\omega_0 = -1/\pi \approx -0.31831$. The dashed line corresponds to the fit of the whole computed range, $x \in [15, 600]$, to a cubic function in $1/\sqrt{x}$. Excluding small values $x < 50$ produces a better fit, as shown by the solid line, for the interval $x \in [100, 600]$. We take this as our estimate, and obtain the error by comparing to the fit in $[50, 400]$. The final values are displayed under the corresponding plots.



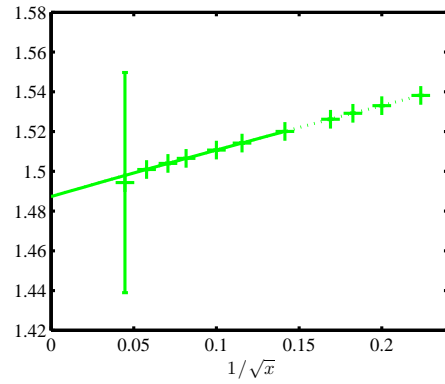
(a) $m/g = 0$, $\frac{M_V}{g} = 0.5642(2)$



(c) $m/g = 0.25$, $\frac{M_V}{g} = 0.5192(5)$

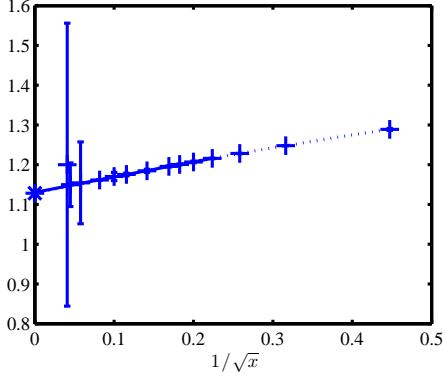


(b) $m/g = 0.125$, $\frac{M_V}{g} = 0.53951(16)$

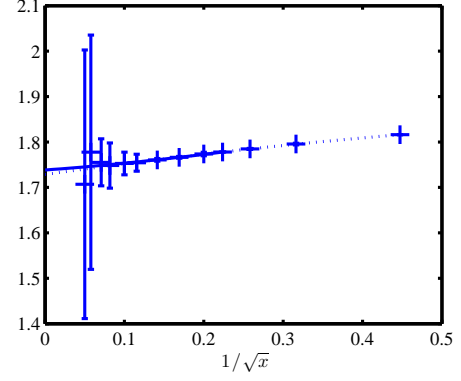


(d) $m/g = 0.5$, $\frac{M_V}{g} = 0.48742(13)$

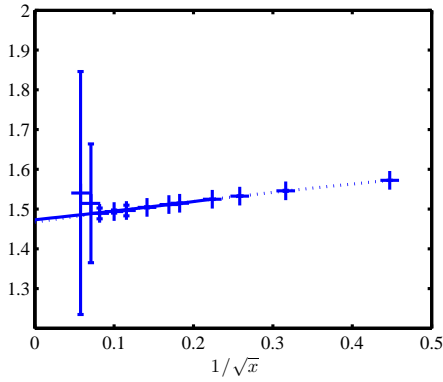
FIG. 6: Energy gap for the vector state, ω_1 , as a function of $1/\sqrt{x}$. The error bars show the uncertainties of the quadratic fits (12) from finite-size scaling. The exact solution for the $m/g = 0$ case, $\omega_1(m/g = 0) = 1/\sqrt{\pi} \approx 0.5641895$ is indicated with a star. Displayed are the fits for the whole interval $x \in [15, 600]$ (dashed line), including up to quadratic terms in $1/\sqrt{x}$, and the same fit for $[50, 400]$ (solid line), but they are practically indistinguishable at the scale of the plots. The errors for large values of x are in this case much more significant due to the smaller D reached for some of the largest system sizes. The most precise fits are in this case found when excluding the last points. In particular, we take the estimate from $x \in [15, 300]$, and we estimate the error by comparing to the fit in $[50, 400]$. The final values for the binding energies, $\frac{M_V}{g}$, are displayed under the corresponding plots.



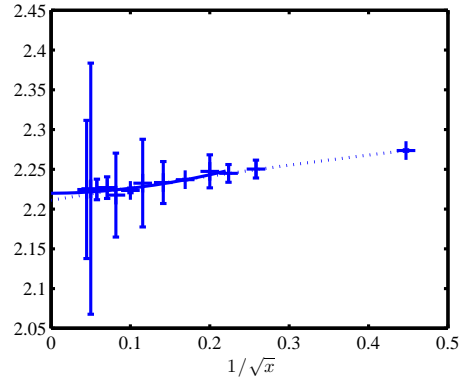
(a) $m/g = 0$, $\frac{M_S}{g} = 1.1283(10)$



(c) $m/g = 0.25$, $\frac{M_S}{g} = 1.239(6)$



(b) $m/g = 0.125$, $\frac{M_S}{g} = 1.221(2)$



(d) $m/g = 0.5$, $\frac{M_S}{g} = 1.213(5)$

FIG. 7: Energy gap for the scalar state, ω_2 , as a function of $1/\sqrt{x}$. The error bars correspond to the uncertainties of the finite-size scaling fits (12). The star on the vertical axes in the $m/g = 0$ plot shows the exact solution $\omega_2(m/g = 0) = 2/\sqrt{\pi} \approx 1.12838$. Fits for the whole range of x (cubic) and for a smaller interval ($x \in [5, 300]$) are shown (respectively dashed and solid lines). As in figure 6, some of the large x estimations have large errors, because they require solving larger systems, for some of which the maximum bond dimension reached was not large enough. Again, we keep as estimate the fit for $x \in [15, 300]$, excluding the very small x , which do not follow the asymptotic behavior, and the larger values of x which have higher errors, and get a rough estimation of the error by comparing to $[30, 200]$ (except in the case $m/g = 0.5$, when due to the larger errors of relatively large x , we compare to the fit in $[15, 200]$).